




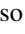






## Slow crystalline electric field fluctuations in the Kondo lattice $\text{SmB}_6$

M. Carlone <sup>1</sup>, J. C. Souza <sup>2,3</sup>, J. Sichelschmidt <sup>3</sup>, P. F. S. Rosa <sup>4</sup>, R. R. Urbano <sup>2</sup>, P. G. Pagliuso <sup>2</sup>, Z. Fisk <sup>4</sup>,  
P. A. Venegas <sup>5</sup>, P. Schlottmann <sup>6</sup> and C. Rettori <sup>2</sup>

<sup>1</sup>POSMAT-Programa de Pós-Graduação em Ciência e Tecnologia de Materiais, Faculdade de Ciências, Universidade Estadual Paulista-UNESP, Bauru, SP, CP 473, 17033-360, Brazil

<sup>2</sup>Instituto de Física “Gleb Wataghin,” Unicamp, 13083-859, Campinas, SP, Brazil

<sup>3</sup>Max Planck Institute for Chemical Physics of Solids, D-01187 Dresden, Germany

<sup>4</sup>Los Alamos National Laboratory, Los Alamos, New Mexico 87545, USA

<sup>5</sup>Departamento de Física, Universidade Estadual Paulista-Unesp, Caixa Postal 473, 17033-360 Bauru, SP, Brazil

<sup>6</sup>Department of Physics, Florida State University, Tallahassee, Florida 32306, USA



(Received 31 January 2022; revised 26 March 2022; accepted 20 April 2022; published 12 May 2022)

This work reports on the temperature dependence of the electron spin resonance (ESR) of  $\text{Gd}^{3+}$ -doped  $\text{SmB}_6$  single crystals at X- and Q-band microwave frequencies in different crystallographic directions. We found an anomalous inhomogeneous broadening of the  $\text{Gd}^{3+}$  ESR linewidth ( $\Delta H$ ) within  $5.3 \text{ K} \leq T \leq 12.0 \text{ K}$  which is attributed to slow crystalline electric field (CEF) fluctuations, slower than the timescale of the used ESR microwave frequencies ( $\sim 10 \text{ GHz}$ ). This linewidth inhomogeneity may be associated to the coupling of the  $\text{Gd}^{3+}$   $S$  states to the breathing mode of the  $\text{SmB}_6$  cage and can be simulated by a random distribution of the 4th CEF parameter,  $b_4$ , that strikingly takes negative and positive values. The temperature at which this inhomogeneity sets in is related to the onset of a continuous insulator-to-metal phase transition. In addition, based on the interconfigurational fluctuation relaxation model, the observed exponential  $T$  dependence of  $\Delta H$  above  $T \simeq 10 \text{ K}$  gives rise to an excitation energy notably close to the hybridization gap of  $\text{SmB}_6$  ( $\Delta \simeq 60 \text{ K}$ ). This charge fluctuation scenario provides important ingredients to the physical properties of  $\text{SmB}_6$ . We finally discuss the interplay between charge and valence fluctuations under the view of slow CEF fluctuations in  $\text{SmB}_6$  by coupling the  $\text{Gd}^{3+}$  ions to the breathing phonon mode via a dynamic Jahn-Teller-like mechanism.

DOI: [10.1103/PhysRevB.105.205116](https://doi.org/10.1103/PhysRevB.105.205116)

### I. INTRODUCTION

The interplay of topology, strongly correlated electrons, and/or magnetism may lead to new quantum states of matter, such as magnetic topological insulators [1], Weyl-Kondo semimetals [2,3], and topological Mott insulators [4]. The first topological phase of matter predicted in a strongly correlated  $f$ -electron system was the topological Kondo insulator (TKI) that resulted in several experimental and theoretical works [5]. In particular,  $\text{SmB}_6$ , a mixed valence compound with a hybridization gap  $\Delta \simeq 60 \text{ K}$  [6,7], is a heavily studied material with disputed experimental results that either support or weaken the TKI scenario [8–13]. In particular, conflicting results are observed when comparing experimental data from samples grown by different routes [14–16]. Nonetheless, it is essential to fully understand the bulk properties of  $\text{SmB}_6$  in order to have a complete description of the possible gapless spin-polarized surface states.

Two intriguing bulk features are the linear low- $T$  specific heat behavior (Sommerfeld coefficient  $\gamma$ ) [17] and “excitonic” states first observed with inelastic neutron scattering and Raman, and used to explain NMR [18,19] and then supported by muon spin relaxation ( $\mu\text{SR}$ ) experiments [20,21]. The lowest reported gamma value is observed in doubly isotope enriched ( $^{154}\text{Sm}^{11}\text{B}_6$ ) samples [22],  $\gamma = 2 \text{ mJ/mol K}^2$ , but the

$\gamma$  value in different growths may vary from  $\gamma = 5 \text{ mJ/mol K}^2$  to about  $25 \text{ mJ/mol K}^2$  [23,24]. Moreover, recent specific heat measurements on  $\text{SmB}_6$  single crystals and powdered samples showed that such finite  $\gamma$  is not related to surface effects but rather of bulk origin [17]. Such observations were interpreted in terms of dispersion of the Majorana Fermi surface as a function of magnetic field that mixes electrons and holes, giving rise to a chargeless “neutral” Fermi surface in the bulk [14,19,25], which may result in a “failed superconductor” [25]. Nevertheless, natural disorder in real materials could also contribute to the thermodynamic properties of the system [26,27].

The neutral particles scenario finds some support in NMR and  $\mu\text{SR}$  experiments. By investigating the  $^{11}\text{B} \pm 3/2 \leftrightarrow \pm 1/2$  transitions, previous NMR studies reported a deviation from an exponential-like activation behavior of the spin-lattice relaxation rate,  $1/T_1$ , at low temperatures ( $6 \text{ K} \leq T \leq 15 \text{ K}$ ) [18,28], which evolves and disappears as function of applied magnetic field. This deviation was interpreted as a result of excitonic in-gap states, namely, magnetic in-gap bound states where antiferromagnetic correlations provide a plausible mechanism for the formation of the magnetic excitons [19,29]. In a similar  $T$  range, low-field ( $H \leq 500 \text{ Oe}$ )  $\mu\text{SR}$  experiments have shown a bulk dynamic magnetic field of magnitude,  $\Delta B = 18 \text{ Oe}$ , and slow timescale of  $t = 60 \text{ ns}$

[20,21]. These authors have also shown that the bulk dynamic magnetic fields are suppressed nearby the surface for SmB<sub>6</sub> single crystals grown by the floating-zone technique. Therefore, Gd<sup>3+</sup> electron spin resonance (ESR) experiments, as a local probe in Gd-doped SmB<sub>6</sub> single crystals, may contribute to elucidate some of these intriguing issues, including the existence of the Sm valence fluctuation (VF), the insulator-to-metal transition, as well as confirming the already reported Jahn-Teller-like effects at low temperature. Gd<sup>3+</sup> couples via ferromagnetic Heisenberg exchange to the conduction electrons, *ce*. The antiferromagnetic Schrieffer-Wolff exchange is much smaller, so that the Gd<sup>3+</sup> ions do not display Kondo effect. Only the valence fluctuations of SmB<sub>6</sub> show a Kondo-like behavior.

Hence this work aims to shed light on the puzzle of the low-temperature ground state of SmB<sub>6</sub> by studying high-quality Sm<sub>1-x</sub>Gd<sub>x</sub>B<sub>6</sub> single-crystalline samples grown by the flux method, by means of the ESR microscopic technique at different frequencies (X band: 9.4 GHz and Q band: 34.1 GHz) in the temperature range of 2.5 K ≤ *T* ≤ 20 K. A highly diluted Gd<sup>3+</sup> doping regime was chosen (*x* = 0.0004) to preclude undesired Gd<sup>3+</sup>-Gd<sup>3+</sup> magnetic interactions.

## II. EXPERIMENTAL DETAILS

Single-crystalline samples of Sm<sub>1-x</sub>Gd<sub>x</sub>B<sub>6</sub> were synthesized by Al-flux-grown technique as described elsewhere [7,30]. The crystals used in our experiments had typical dimensions of ~700 μm × 300 μm × 120 μm and estimated skin depth δ ≈ 100 μm at *T* ≤ 4 K (δ = √ρ/πνμ). Magnetic susceptibility measurements were carried out in a SQUID vibrating-sample magnetometer. ESR measurements in as-grown facets of cubic single crystals were performed in X- (9.4 GHz) and Q-band (34.1 GHz) spectrometers equipped with a goniometer and a He-gas flow cryostat able to vary the temperature within the range of 2.5 K ≤ *T* ≤ 20 K. The studied single crystals were not polished but etched before the ESR measurements in a 3:1 mixture of hydrochloric and nitric acids (aqua regia) to remove residual impurities on their surfaces due to the Al flux. The studied sample masses ranged from 0.3 to 4.0 mg. In this report the concentration *x* refers to the nominal concentration value of *x* = 0.0004. Its actual concentration of *x* = 0.00034(1) was determined by ESR measurements using a standard weak pitch sample (0.79 · 10<sup>14</sup> spins/cm<sup>3</sup>) [31].

## III. THEORETICAL MODEL

The absorption response with exchange narrowing effects due to the exchange interaction between the Gd<sup>3+</sup> local moment and the *ce* is obtained by calculating the transverse dynamic susceptibility χ<sup>+</sup>(ω). Assuming no bottleneck relaxation effects, χ<sup>+</sup>(ω) can be approximated by [32–35]

$$\chi^+(\omega) \approx 1 - \omega_0 \sum_{M',M} [P_M(\Omega^{-1})_{M,M'}], \quad (1)$$

where *P<sub>M</sub>* are the transition probabilities between the *M* ↔ *M* + 1 states and can be written as

$$P_M = C_M \exp^{M\hbar\omega_0/kT} / \sum_{M'} C_{M'} \exp^{M'\hbar\omega_0/kT}. \quad (2)$$

The coefficients *C<sub>M</sub>* are defined as *C<sub>M</sub>* = *S*(*S* + 1) – *M*(*M* + 1), with *M* and *M'* the quantum numbers associated with the Gd<sup>3+</sup> (*S* = 7/2) Zeeman split states. Ω<sub>*M,M'*</sub> is the transition matrix, which can be written as

$$\begin{aligned} \Omega_{M,M'} = & [H_0 - H - H_M] \delta_{M,M'} - i \delta_{M,M'} \Delta H_{\text{res}} \\ & - i(1/2) \Delta H C_M [2\delta_{M,M'} - \delta_{M,M'+1} - \delta_{M,M'-1}]. \end{aligned} \quad (3)$$

The real part of the diagonal elements contains the resonance field, and the remaining imaginary term corresponds to the ESR relaxation of Gd<sup>3+</sup> ions. In this equation, *H*<sub>0</sub> = ħω<sub>0</sub>/gμ<sub>B</sub>, with ω<sub>0</sub> being the microwave frequency and Δ*H*<sub>res</sub> the residual linewidth. Δ*H* is associated to *T*-dependent relaxation processes, where the diagonal terms are responsible for the ESR linewidth, and the off-diagonal elements contain the fluctuation rates of the local moments between two consecutive resonance fields and are responsible for the narrowing effects of the fine structure.

The Gd<sup>3+</sup> ESR spectrum in an insulating host presents a fine structure of seven Lorentzian resonances due to the crystal electric field (CEF) on Gd<sup>3+</sup> ions located at cubic sites. The spectrum is then calculated using the well-known CEF Hamiltonian for cubic symmetry in the presence of a magnetic field [36,37],

$$\mathcal{H} = g\mu_B \mathbf{H} \cdot \mathbf{S} + (1/60)b_4(O_4^0 + 5O_4^4), \quad (4)$$

where the first term is the Zeeman interaction with μ<sub>B</sub> the Bohr magneton, *b*<sub>4</sub> the fourth-order CEF parameter, and *O*<sub>4</sub><sup>*n*</sup> the fourth-order Stevens operators. The contribution of the sixth-order CEF term is negligible and has not been considered for simplicity.

In a cubic environment, the fine-structure resonance fields, including their angular dependence, are

$$H_M = (1/60)b_4 p(\theta) \langle M | O_4^0 + 5O_4^4 | M \rangle, \quad (5)$$

with *p*(θ) = 1 – 5[sin<sup>2</sup>θ – (3/4)sin<sup>4</sup>θ] being the angular dependence for cubic symmetry, and θ the angle between the applied magnetic field and the crystallographic axis. In this work, the applied magnetic field *H* is always rotated within the (110) plane.

However, in a metallic host, the absorption is given by the real part of the impedance, that is, *P* ∝ Re(χ<sup>+</sup>(ω)) – Im(χ<sup>+</sup>(ω)) [33,38]. The transverse dynamic susceptibility χ<sup>+</sup> is obtained from Eq. (1), which includes all the narrowing effects of the fine structure. The elements of the transition matrix are calculated using Eqs. (4) and (5).

The linewidth and *g* value are extracted from the simulated spectra using an admixture of absorption (χ'') and dispersion (χ') of Lorentzian line shapes [39,40], which gives for the absorption derivative,

$$\frac{d[\xi \chi' + (1 - \xi) \chi'']}{dH} \propto \frac{\xi(1 - x^2)}{(1 + x^2)^2} + \frac{2(1 - \xi)x}{(1 + x^2)^2}, \quad (6)$$

where *x* = (*H*<sub>0</sub> – *H*)γ<sub>e</sub>*T*<sub>2</sub>, γ<sub>e</sub> is the electron gyromagnetic ratio, and *T*<sub>2</sub> is the spin-spin relaxation time. For ξ = 0 we have pure absorption, for ξ = 1 pure dispersion, and for 0

$\leq \xi \leq 1$  the well-known Dysonian asymmetric ESR resonance line shape [41].

Using Eqs. (1)–(5), it is possible to fully describe the fine structure of  $\text{Gd}^{3+}$ , including the exchange narrowing effects. However, in order to describe the inhomogeneous broadening of each resonance of the fine structure, slow fluctuations of the CEF (slower than  $\sim 10$  GHz, the frequency of our ESR experiments) will be considered through a  $T$ -dependent Gaussian distribution of the CEF  $b_4$  parameter (GDCEF) with standard deviation  $\sigma_{b_4}$ . The origin for these slow CEF fluctuations will be associated to the coupling of the  $\text{Gd}^{3+}$   $S$  states to the breathing mode of the  $\text{SmB}_6$  cage (see below) [42,43].

To search for a set of parameters that fits all ESR experimental spectra we used the global optimization method, generalized simulated annealing [44]. We did that for all  $H$  directions and temperatures. In particular, the simulations at low temperature, where the spectra are resolved, permit verification of the cubic symmetry of the crystal and provide very accurate values for  $b_4$ ,  $\Delta H_{\text{res}}$ , and  $g$ . Through the simulation of the thermal evolution of the spectra, the parameters  $\xi$ ,  $b$ , and the VF parameters are obtained.

#### IV. RESULTS AND DISCUSSION

Figure 1 shows the X-band (9.4 GHz)  $\text{Gd}^{3+}$  experimental ESR spectra for  $\text{Sm}_{0.9996}\text{Gd}_{0.0004}\text{B}_6$  with the external magnetic field  $\mathbf{H}_0$  applied along the [001] and [110] directions at 4.6 and 4.5 K, respectively. The red solid lines in Fig. 1 are the simulated  $\text{Gd}^{3+}$  fine structure of the spectra for both cases using seven Lorentzian lines. Because the skin depth is of the order of the crystal dimensions at these temperatures, it is natural that the line shape of each individual resonance resembles an insulating host. Even at 34.1 GHz (Q band) it was not possible to capture the skin depth conductivity effects in this sample [31,45,46]. Note that at lower  $x = 0.0002$  [47] and higher  $x = 0.02$  [31] also, diffusivelike and Dysonian line shapes were respectively reported. The obtained CEF parameters are roughly the same in both cases:  $b_4 = (-9.9 \pm 1.2)$  Oe;  $g = (1.912 \pm 0.003)$  for  $H \parallel [001]$  and  $b_4 = (-9.0 \pm 1.2)$  Oe;  $g = (1.912 \pm 0.002)$  for  $H \parallel [110]$ . Besides, quite narrow residual linewidths were considered in these simulations, i.e.,  $\Delta H_{\text{res}}^{[001]} = (19.5 \pm 1.0)$  Oe and  $\Delta H_{\text{res}}^{[110]} = (17.4 \pm 0.9)$  Oe.

In order to study the  $T$  evolution of the ESR fine structure in a mixed valence insulator, one should also consider the  $T$ -dependent relaxation process due to the VF between the  $4f^n$  and  $4f^{n+1}$  configurations of Sm ions. This causes a fast fluctuating field at the  $\text{Gd}^{3+}$  site [34,48–50] which homogeneously broadens the linewidth of the individual resonances, leading to the narrowing of the  $\text{Gd}^{3+}$  CEF fine structure.

We have calculated the individual linewidth  $\Delta H(T)$ , at any orientation, using a  $T$ -independent residual linewidth and homogeneous  $T$ -dependent contributions due to Korringa and Sm VF relaxation mechanism processes as follows [50]:

$$\Delta H = bT + Ae^{-E_{\text{ex}}/T}, \quad (7)$$

where the first term is the usual Korringa relaxation rate [51] associated to the possible presence of a relaxation process due

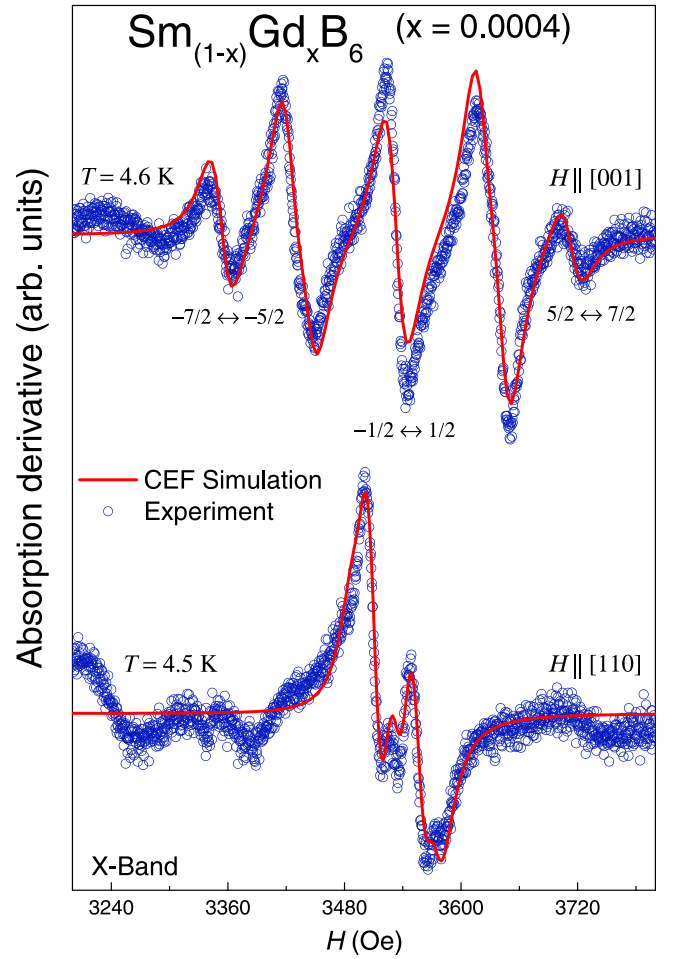


FIG. 1. X-band  $\text{Gd}^{3+}$  ESR spectra for  $\text{Sm}_{0.9996}\text{Gd}_{0.0004}\text{B}_6$  with  $H \parallel [001]$  and  $H \parallel [110]$  at nearly 4.5 K [31]. The solid red lines are simulations using Eqs. (4) and (5) considering  $\text{Gd}^{3+}$  ions in a cubic insulating matrix without the influence of the GDCEF.

to the exchange interaction,  $J_{fs}$ , between the  $\text{Gd}^{3+}$  localized magnetic moment and the  $ce$ . The last term is the exponential contribution to the  $\text{Gd}^{3+}$  relaxation due to the  $\text{Sm}^{2.6+}$  VF [50], where  $A$  is a constant and  $E_{\text{ex}}$  is the interconfigurational excitation energy, i.e., the energy necessary to exchange an electron between the  $ce$  band and the Sm  $4f$  states [34,50]. Actually,  $E_{\text{ex}}$  is the energy to excite an electron from the hybridized valence band into the hybridized conduction band (indirect gap). Figures 2(a) and 2(b) show the  $T$  evolution of the X-band  $\text{Gd}^{3+}$  ESR spectra shown in Fig. 1, where we have used Eq. (7) to describe the  $T$  evolution of the linewidth for each component of the fine structure. The parameters obtained for the spectra in Fig. 1 were further confirmed by the ESR spectra taken at  $H$  nearly  $30^\circ$  from the [001] direction in the (110) plane where the cubic fine structure is about to collapse, as shown in Fig. 3(a) at 4.2 K. These simulations were able to capture most of the expected details of the cubic CEF fine structure of the ESR spectra for quite isolated  $\text{Gd}^{3+}$  ions in  $\text{SmB}_6$ , confirming the high dilution of our single crystals.

Therefore,  $\text{SmB}_6$  behaves as an insulator at low temperatures ( $T \leq 6$  K), and the  $\text{Gd}^{3+}$  ESR spectra are well described by Eq. (4), with narrow residual linewidths,  $\Delta H_{\text{res}}$ . Yet at

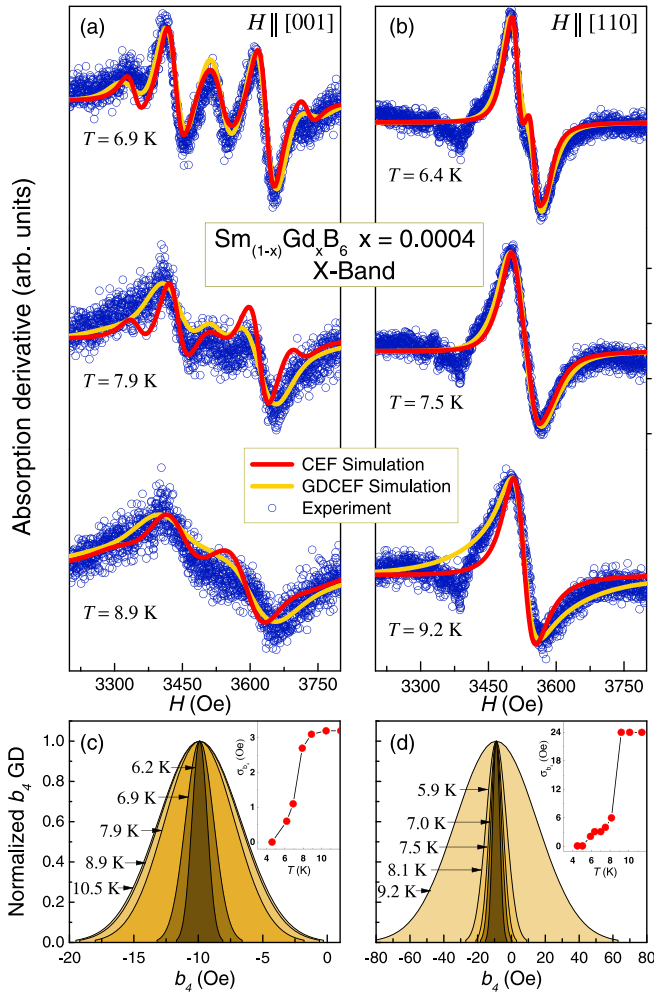


FIG. 2.  $T$  dependence of X-band  $\text{Gd}^{3+}$  ESR spectra for (a)  $H \parallel [001]$  and (b)  $H \parallel [110]$ . The yellow and red solid lines are the best simulations of the  $\text{Gd}^{3+}$  ESR spectra, with and without the influence GDCEF, respectively. (c) and (d) present the GDCEF for both cases, and the insets show the  $T$  dependence of their standard deviations  $\sigma_{b_4}$ .

the insulator-to-metal crossover temperature and above ( $T \gtrsim 6\text{K}$ ), due to the presence of  $ce$  and Sm VF, one must also take into account contributions from the Korringa and Sm VF relaxation processes to the ESR linewidth. Nevertheless, at the intermediate temperatures ( $5.3\text{K} \leq T \leq 12\text{K}$ ) highlighted in Fig. 4, these contributions were not able to simulate the experimental ESR spectra satisfactorily, as shown by red solid lines in Figs. 2(a) and 2(b).

In order to account for the discrepancy between experiment and calculation, an inhomogeneous linewidth broadening through the GDCEF, with a  $T$ -dependent standard deviation,  $\sigma_{b_4}$ , was considered in our simulations. The yellow solid lines in Figs. 2(a) and 2(b) are the best simulations of the  $\text{Gd}^{3+}$  ESR spectra caused by this GDCEF. The improvement of the agreement between simulation and data is noticeable. Figures 2(c) and 2(d) show the  $T$  dependence of the GDCEF used to simulate the spectra of Figs. 2(a) and 2(b), respectively. Notice that the  $b_4$  CEF parameter distribution, which reproduces all the features of the experimental spectra, depends on the field direction.

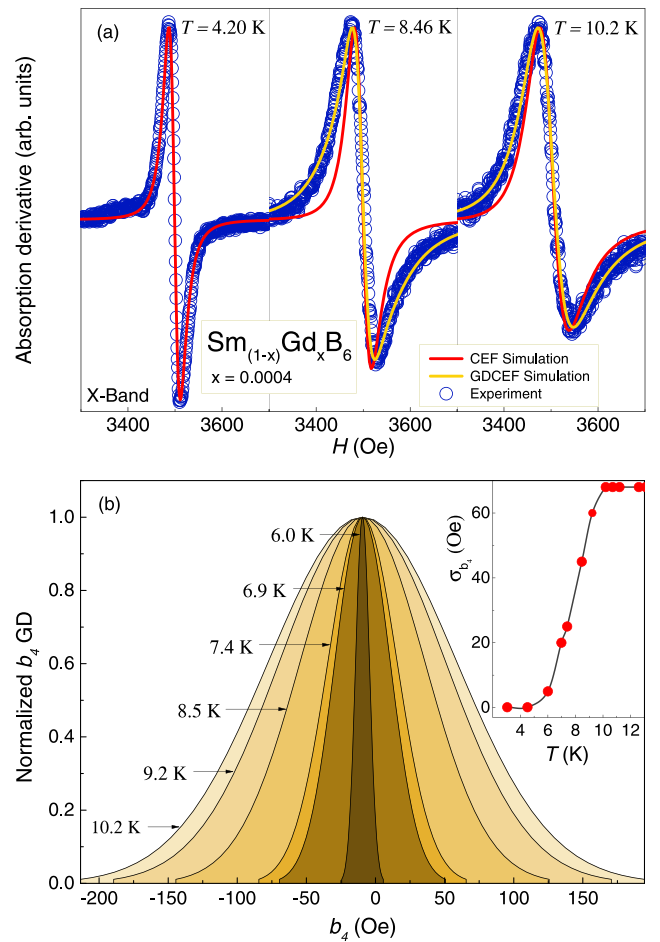


FIG. 3. (a) X-band  $T$  dependence of the  $\text{Gd}^{3+}$  ESR line shapes nearly the angle of collapsed fine structure  $\theta_0$ . The yellow and red solid lines are simulations with and without GDCEF, respectively. All three spectra are on the same scale. (b) Gaussian distribution of  $b_4$  (GDCEF) used to simulate the nearly collapsed ESR spectra at different temperatures. The inset shows the  $T$  dependence of the GDCEF standard deviation  $\sigma_{b_4}$ .

The presence of an inhomogeneous distribution of  $b_4$  can be further confirmed by a thorough analysis of the  $\text{Gd}^{3+}$  ESR spectra for the field direction where the CEF fine structure collapses into one single resonance line. For cubic symmetry the fully collapsed fine structure occurs at  $\theta_0 = 29.67^\circ$  from the  $[001]$  direction in the  $(110)$  plane, i.e.,  $p(\theta_0) = 0$  in Eq. (5). At this angle there is no contribution to the position of the spectra from CEF effects. Hence, the seven  $\text{Gd}^{3+}$  ESR resonances overlap at the resonance field of the  $(+1/2 \leftrightarrow -1/2)$  transition and the whole ESR spectrum behaves as an effective spin  $S = 1/2$ . Nonetheless, in real experiments a perfect alignment of the magnetic field along the collapsed angle is difficult to achieve. Due to field misorientation and/or crystal defects, a small misalignment is always left in; therefore,  $p(\theta) \neq 0$ . Thus, even though the observed spectrum presents a single resonance, its linewidth will be always inhomogeneously broadened by CEF effects. This small misalignment would allow perception of any linewidth anomaly caused by an even tiny CEF effect. The  $\text{Gd}^{3+}$  CEF is then the central issue in the interpretation of the spectra.

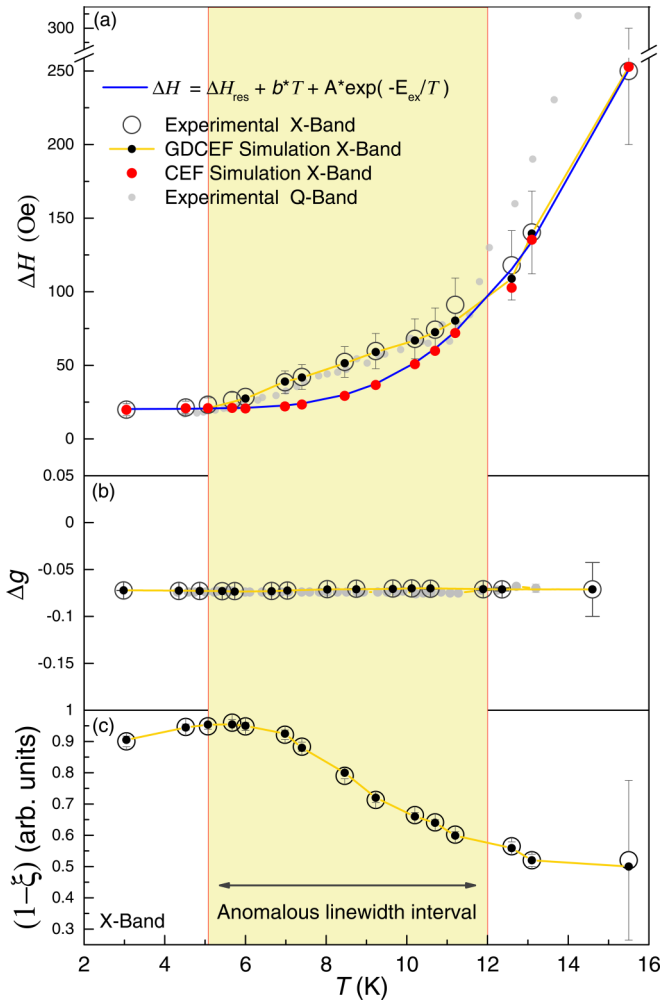


FIG. 4. (a)  $T$  dependence of the  $\text{Gd}^{3+}$  ESR linewidth for X (empty black circles) and Q (solid gray dots) bands, at  $H \parallel 30^\circ$ : the angle of nearly collapsed fine structure. The theoretical simulations with GDCEF (solid black dots and yellow solid line), without GDCEF (solid red dots), and by Eq. (7) (solid blue line). The used parameters were  $\Delta H_{\text{res}} = 20$  Oe,  $E_{\text{ex}} = 60$  K, and above the insulator-to-metal transition, a Korringa rate of  $b = 0.1$  Oe/K. (b) The  $g$  shift,  $\Delta g$ , for X and Q bands as a function of temperature. (c)  $T$  evolution of the line-shape asymmetry parameter  $(1 - \xi)$ . The yellowish band in the background highlights the anomalous linewidth interval ( $5.3 \text{ K} \leq T \leq 12.0 \text{ K}$ ).

Figure 3(b) shows the  $T$  evolution of the GDCEF used to simulate the  $T$  dependence of the nearly collapsed spectra of Fig. 3(a) in the  $T$  interval ( $5.3 \text{ K} \leq T \leq 12.0 \text{ K}$ ), which is in Fig. 4 denoted by the yellowish band. The experimental  $T$  dependence of the ESR spectrum and their respective simulations, with (solid yellow lines) and without (solid red lines) GDCEF, are also presented. Notice the smooth change of the ESR spectra. The linewidth broadens, caused by the slow dynamic CEF fluctuation, and the line shape goes from pure Lorentzian to Dysonian due to the decrease of the skin depth as a consequence of the conductivity increase in this anomalous linewidth temperature interval [31].

Figure 4(a) shows the  $T$  dependence of the X- and Q-band  $\text{Gd}^{3+}$  ESR linewidth near the collapsed angle for

$\text{Sm}_{0.9996}\text{Gd}_{0.0004}\text{B}_6$ . In the absence of a  $b_4$  GDCEF contribution to the linewidth [red solid circles in Fig. 4(a)], we obtain  $E_{\text{ex}} = 60$  K, which is close to the  $\text{SmB}_6$  hybridization gap [7]. We used  $\Delta H_{\text{res}} \approx 20$  Oe, and as expected, there is no Korringa relaxation rate at low  $T$ , but a small one,  $b = 0.1(1)$  Oe/K, is observed for  $T$  above 8 K, consistent with the bulk conductivity [7,31] that sets in near this temperature.

In Fig. 4(c) we present the  $T$  dependence of the asymmetry parameter,  $\xi$ , of our ESR results. The ESR resonances of Fig. 3(a) clearly display a change from insulator [ $(1 - \xi) \approx 1$ ] to metallic [ $(1 - \xi) \approx 0.55$ ] line-shape symmetry within the temperature interval where anomalous broadening is observed. It was shown that the line shape evolves from a symmetric Lorentzian to an asymmetric Dysonian upon temperature increase. This behavior, together with an enhanced conductivity, is associated with a monotonic crossover from insulator-to-metal phases occurring within  $6 \text{ K} \leq T \leq 12 \text{ K}$  and provides strong evidence for the local closure of the hybridization gap, caused in part by the electron-phonon (rattling) interactions [34].

The linewidth behavior according to Eq. (7) and shown in Fig. 4(a) describes reasonably well the  $\text{Gd}^{3+}$  ESR linewidth in the low- $T$  and high- $T$  regimes. However, in the temperature interval of the anomalous linewidth, there is an evident discrepancy between the experimental linewidth and that predicted by the VF model alone. Using VF, Korringa relaxation, and a  $T$ -dependent GDCEF of  $b_4$ , the experimental line shape and linewidth are both well reproduced in that temperature range for this particular magnetic field orientation [Figs. 3(a) and 4(a)]. There was no need to consider any  $\text{Gd}^{3+}$  spin-spin exchange contribution in these simulations, which is further consistent with the extreme low Gd concentration in these single crystals.

It is remarkable that the anomalous linewidth temperature interval coincides with the anomalous impedance regime found in a low- $T$  impedance spectroscopy study of  $\text{SmB}_6$  single crystals that leads to a current controlled negative differential resistance [43]. A possible connection with the parameter  $\xi$  is presented in the Appendix.

As illustrated in Fig. 3(b),  $\sigma_{b_4}$  increases dramatically inside the anomalous interval. This behavior is also evident in the inset of this figure where  $\sigma_{b_4}$  rises until stabilizing near  $T \approx 10$  K. For higher  $T$ , the contribution of the GDCEF to the inhomogeneous linewidth is overcome by the Korringa and VF narrowing effects. Hence the ESR linewidth is then consistently described by Eq. (7). It is worth mentioning that similar behavior can be also verified in the other field orientations. Notice, however, that the increase of  $\sigma_{b_4}$ , although evident, is less pronounced when  $H$  is applied along [001] and [110]. This is because when  $H \parallel 30^\circ$ , the spectra is about to collapse and the same Gaussian distribution causes, obviously, at any other orientation, a distinct linewidth increase of the individual resonances due to a static inhomogeneous broadening caused by the presence of crystal defects.

We shall point out that the GDCEF of  $b_4$  used to simulate the ESR spectra takes into account either positive and negative values of  $b_4$  [Figs. 2(c), 2(d) and 3(b)]. Experimentally, it is verified that usually rare-earth-doped insulating materials present negative  $b_4$  values, while conductors present the positive ones [35,52]. To the best of our knowledge,  $\text{SmB}_6$  is the

first compound where negative and positive values of  $b_4$  may coexist at a nanometer scale, with temperature playing the role of the control parameter. For the Kondo insulator  $\text{SmB}_6$ , positive and negative values of  $b_4$  may indicate the presence of a heterogeneous phase where metallic and insulating regions coexist in this  $T$  range as a consequence of a local loss of coherence between the hybridized  $d$ - $ce$  and  $\text{Sm-}4f$  electrons due to the CEF fluctuations. It is worth mentioning that this heterogeneous phase is quite different than that observed for  $\text{Gd}^{3+}$ -,  $\text{Er}^{3+}$ -, and  $\text{Eu}^{2+}$ -doped  $\text{CaB}_6$  at much higher concentrations, where donor bound states percolate to build up the metallic regions [53,54].

In Appendix B we present a dynamic Jahn-Teller-like model explaining the slow time-dependent variations of the cubic CEF parameter  $b_4$  giving rise to insulating and metallic values for  $b_4$ . Superposition of  $\Gamma_1$  oscillation modes could yield distributions as in Figs. 2 and 3.

Another possible origin for the linewidth anomaly could be a slow  $g$ -value fluctuation, but this is ruled out by ESR experiments carried out in different microwave frequencies, 9.4 and 34.1 GHz, which, within the accuracy of the experiments, presented the same  $\Delta H(T)$  [Fig. 4(a)] and  $T$ -independent  $g$  shift [Fig. 4(b)] [37].

The  $g$  shift,  $\Delta g = g_{\text{exp}} - g_{\text{ins}}$ , calculated with respect to the  $g$  value of isolated  $\text{Gd}^{3+}$  ions in insulators ( $g_{\text{ins}} = 1.993$ ), is presented in Fig. 4(b) [37]. The negative  $\Delta g$  measured in X and Q bands are nearly  $T$  independent and is probably associated with the covalent antiferromagnetic coupling between the donor bound state to the  $\text{Gd}^{3+}$  impurity [55]. Therefore the observed linewidth anomaly cannot be attributed to magnetic spin-spin interactions among the  $\text{Gd}^{3+}$  ions. We should also point out that the slow magnetic field dynamics observed by  $\mu\text{SR}$  experiments at low  $T$  and low  $H$  is disregarded here because it vanishes at the temperature and field ranges used in our ESR experiments [20,21].

Moreover, a weak and broad additional dispersionless mode was observed in the energy gap between the acoustic and optical modes due to the nonadiabatic interaction of phonons [56]. Notice that the small  $\text{Sm}^{2.6+}$  ions may experience anharmonic rattling vibrations at interstitial positions of the large lattice cage of  $\text{SmB}_6$  [42]. This is probably the responsible mechanism for the observed dispersionless mode. Thus, since lattice vibrations (phonons) are expected to interfere strongly with the Sm fluctuation valence because of their nearly coincident characteristic times ( $10^{12} \text{ s}^{-1}$ -phonons to  $10^{15} \text{ s}^{-1}$ -VF) [56–58], it is conceivable that slow charge fluctuations, leading to slow CEF fluctuations, result from the interfering beating between these two fast phenomena of close frequencies. Moreover, inelastic neutron-scattering experiments demonstrated the existence of magnetic in-gap bound states in  $\text{SmB}_6$  [59,60]. Also, two dispersionless magnetic excitation at energies  $h\nu_1 \simeq 36$  and  $\simeq 14$  meV were confirmed within the direct gap of  $\text{SmB}_6$ . Under this scenario, the  $T$ -dependent high-field NMR measurements of the  $^{11}\text{B}$  Knight shift and spin-lattice relaxation rates showed a marked decrease of  $1/T_1$  with increasing  $H$  for  $T \leq 10$  K. Hence, the progressive suppression of the spin-lattice relaxation channel upon high fields suggests that the magnetic in-gap bound states do play an important role in this process [18,28].

Nevertheless, nuclear relaxation due to slow charge fluctuations of the CEF gradients was disregarded by isotopic effect based on similar  $^{10}\text{B}$  and  $^{11}\text{B}$  NMR results, and the nature of the nuclear spin-lattice relaxation was assumed to be purely magnetic [61]. In contrast to NMR, the ESR results presented in this work did not capture any magnetic effects as revealed by the  $T$ -independent  $g$ -shift reported in Fig. 4(b).

## V. CONCLUSION

In summary, we have performed frequency and  $T$ -dependent ESR experiments in the  $\text{Gd}^{3+}$ -doped  $\text{SmB}_6$  Kondo insulator compound with  $x_{\text{Gd}} \simeq 0.0004$  and magnetic field applied in different crystallographic directions. Based on the interconfigurational VF model, narrowing effects on the  $\text{Gd}^{3+}$  ESR fine structure at different crystallographic directions was clearly seen [Figs. 2(a) and 2(b)]. For  $H$  close to  $\theta_0$ , near the collapsed fine structure, the ESR linewidth follows the expected exponential-like behavior, yielding an activation energy of  $\simeq 60$  K, comparable with the Kondo hybridization gap of  $\text{SmB}_6$ . However, in the temperature interval of  $5.3 \text{ K} \leq T \leq 12.0 \text{ K}$ , an anomalous and inhomogeneous contribution to the ESR linewidth is observed, which was accounted by a  $T$ -dependent GDCEF of the  $b_4$  parameter in Eq. (4). This theoretical framework was able to mimic the slow CEF fluctuations (slower than  $\sim 10$  GHz) and reproduce the anomalous linewidth broadening observed in this  $T$  interval.

In this  $T$  interval a crossover from insulator to metallic environment is observed and coincides with anomalies of the impedance of  $\text{SmB}_6$ , as is discussed in Appendix A. In Appendix B we present a dynamic Jahn-Teller-like model by coupling the  $^8\text{S}$  states of  $\text{Gd}^{3+}$  to the cage breathing mode, which can explain the slow fluctuations of  $b_4$  with positive and negative values of  $b_4$ . This corresponds to fluctuations with time of the crystalline CEF parameter  $b_4$ . The amplitude of the J-T oscillation increases with temperature. Hence, in Fig. 4(a),  $\Delta H$  keeps increasing with  $T$  above 12 K. Our simulations indicate the coexistence of positive and negative  $b_4$  values, suggesting the existence of a heterogeneous phase of metallic and insulating regions. We have shown that our ESR data can be fully explained by assuming a slow CEF fluctuation concomitantly with fast phonon and VF effects.

Our work introduces a perspective regarding the enigmatic properties of  $\text{SmB}_6$ , showing that the interplay between fast VF and phonons give rise to slow charge fluctuations that provide an important clue for the understanding of the physical properties in this  $\text{SmB}_6$  Kondo system. Nonetheless, further theoretical work is required to fully understand the mechanism involved in the interplay between slow CEF fluctuation, phonons, and VF in  $\text{SmB}_6$ . Besides, it is possible that slow CEF fluctuations associated to anharmonic dynamic Jahn-Teller of Sm rattling oscillations [42] may be observed at low  $T$  as a barely perceptible anomaly in the  $^{149}\text{Sm}$  quadrupole synchrotron radiation Mossbauer spectra [62–64], then giving further support to the existence of slow CEF fluctuations at low- $T$  in  $\text{SmB}_6$ .

Finally, we believe that our ESR results in the  $\text{Gd}^{3+}$ -doped  $\text{SmB}_6$  Kondo insulator have captured relevant features of this

system, i.e., valence fluctuation, phonons, charge fluctuations, and  $T$ -dependent hybridization gaps [18,20,21,28,29,34,56].

### ACKNOWLEDGMENTS

This work was supported and performed under the auspices of FAPESP (SP-Brazil) through Grants No. 2020/12283-0 2018/11364-7, No. 2017/10581-1, No. 2013/17427-7, No. 2012/04870-7, and No. 2012/05903-6; CNPq (Brazil) Grants No. 309483/2018-2, No. 442230/2014-1, and No. 304496/2017-0; CAPES (Brazil); and FINEP (Brazil). The work at Los Alamos National Laboratory (LANL) was performed under the auspices of the U.S. Department of Energy, Office of Basic Energy Sciences, Division of Materials Science and Engineering.

### APPENDIX A: LOW- $T$ IMPEDANCE OF $\text{SmB}_6$

The dielectric response of  $\text{SmB}_6$  at low  $T$  can be divided into three temperature regimes: (i) for  $T < 4$  K only the topological surface states conduct while the bulk states are frozen out, (ii) for  $T > 10$  K the conduction is predominantly through the activated semiconductor states, and (iii) in the nontrivial intermediate regime, both channels participate in the transport.

The equivalent circuit for the system consists of a resistor  $R_b$  and a capacitor  $C_b$  connected in parallel to parametrize the insulating bulk and a parallel connection of a resistor  $R_s$  and an inductor  $L_s$  for the impedance of the surface states. The surface and bulk elements are, of course, connected in parallel. The impedance of  $\text{SmB}_6$  platelets has recently been measured by Stankiewicz *et al.* [43] in the relevant  $T$  range up to 15 K. The voltage and current are out of phase, giving rise to Lissajous curves [8] in the intermediate region (iii), and for very thin  $\text{SmB}_6$  film a negative differential resistance leads to self-sustained voltage oscillations at low  $T$  [8,65,66] as a consequence of Joule heating. The intermediate  $T$  region (iii), corresponds approximately to the anomalous linewidth temperature interval in Fig. 4.

The quantity  $(1 - \xi)$  in Fig. 4(c) indicates the temperature where the crossover from an insulating to a metallic phase takes place. This agrees with the temperature where the deviation between the experimental X-band data and CEF

simulation becomes evident [see Fig. 4(a)]. The anomalies in the ESR spectra are therefore related to the anomalies in the impedance of  $\text{SmB}_6$ . The deviations of  $(1 - \xi)$  are consistent with the Joule heating.

### APPENDIX B: COUPLING TO LATTICE VIBRATIONS

In a cubic environment there are vibrations of symmetry  $\Gamma_1$ ,  $\Gamma_3$ , and  $\Gamma_5$  that in principle can couple to an impurity. The  $\Gamma_3$  and  $\Gamma_5$  are degenerate and give rise to a Mexican hat, which lifts the degeneracy, while the  $\Gamma_1$  mode is nondegenerate. In Ref. [42] we considered the dynamic Jahn-Teller effect of  $\text{Er}^{3+}$  ions in  $\text{SmB}_6$  with phonons of  $\Gamma_3$  symmetry. In the case of  $\text{Gd}^{3+}$  (an S state), the mode of  $\Gamma_1$  symmetry (breathing mode) can couple without breaking the cubic symmetry but giving rise to a time-dependent  $b_4$ . The coupling of the  $\Gamma_3$  and  $\Gamma_5$  modes gives rise to tetragonal and trigonal spin-lattice coefficients, respectively [67].

The unperturbed half-filled  $4f^7$  shell of  $\text{Gd}^{3+}$  has a  $^8S_{7/2}$  ground state. Perturbations are the spin-orbit interaction and the cubic CEF Hamiltonian. The perturbation expansion up to fourth order in the spin-orbit coupling ( $\xi_{so} = 1480 \text{ cm}^{-1}$ ) was carried out by Wybourne [68]:

$$0.98655|^8_7S\rangle + 0.16176|^6_5P\rangle - 0.01232|^6_7D\rangle \\ + 0.00100|^6_5F\rangle - 0.00014|^6_7G\rangle, \quad (\text{B1})$$

leading to a reduced  $g$  factor of 1.99454. Here the left-hand superscript is  $2S + 1$  of the multiplet and the left-hand subscript is the seniority number [69]. The cubic CEF parameter  $b_4$  is now obtained as the matrix element of the CEF Hamiltonian with the wave function Eq. (B1).

The static  $b_4$  is given by the point-charge model for the CEF. In addition, one needs to consider the screening of the ionic charges by the  $ce$ , which reduces the CEF effect. The breathing-mode phonon changes the size of the  $B_6$  cage without destroying the symmetry. This gives rise to a modulation of  $b_4$  with time and hence to a distribution of  $b_4$  values at a given time. If this modulation is large enough, the system could have some regions with negative  $b_4$  as for an insulator and others with positive  $b_4$  as for a conductor. Since the breathing mode is larger than the size of a unit cell, it is to be expected that it arises from the acoustic branches in  $\text{SmB}_6$ . Hence, the time dependence of the modulation of  $b_4$  is rather slow.

- 
- [1] R. S. K. Mong, A. M. Essin, and J. E. Moore, *Phys. Rev. B* **81**, 245209 (2010).  
 [2] P.-Y. Chang and P. Coleman, *Phys. Rev. B* **97**, 155134 (2018).  
 [3] H.-H. Lai, S. E. Grefe, S. Paschen, and Q. Si, *Proc. Natl. Acad. Sci.* **115**, 93 (2018).  
 [4] D. Pesin and L. Balents, *Nat. Phys.* **6**, 376 (2010).  
 [5] M. Dzero, J. Xia, V. Galitski, and P. Coleman, *Annu. Rev. Condens. Matter Phys.* **7**, 249 (2016).  
 [6] J. C. Cooley, M. C. Aronson, Z. Fisk, and P. C. Canfield, *Phys. Rev. Lett.* **74**, 1629 (1995).  
 [7] Y. S. Eo, A. Rakoski, J. Lucien, D. Mihailov, Ç. Kurdak, P. F. S. Rosa, and Z. Fisk, *Proc. Natl. Acad. Sci.* **116**, 12638 (2019).  
 [8] D. J. Kim, J. Xia, and Z. Fisk, *Nat. Mater.* **13**, 466 (2014).  
 [9] D. J. Kim, S. Thomas, T. Grant, J. Botimer, Z. Fisk, and J. Xia, *Sci. Rep.* **3**, 3150 (2013).  
 [10] P. Hlawenka, K. Siemensmeyer, E. Weschke, A. Varykhalov, J. Sánchez-Barriga, N. Y. Shitsevalova, A. V. Dukhnenko, V. B. Filipov, S. Gabáni, K. Flachbart, O. Rader, and E. D. L. Rienks, *Nat. Commun.* **9**, 517 (2018).  
 [11] S. Wolgast, Ç. Kurdak, K. Sun, J. W. Allen, D.-J. Kim, and Z. Fisk, *Phys. Rev. B* **88**, 180405(R) (2013).  
 [12] H. Herrmann, P. Hlawenka, K. Siemensmeyer, E. Weschke, J. Sánchez-Barriga, A. Varykhalov, N. Y. Shitsevalova, A. V. Dukhnenko, V. B. Filipov, S. Gabáni, K. Flachbart, O. Rader,

- M. Sterrer, and E. D. L. Rienks, *Adv. Mater.* **32**, 1906725 (2020).
- [13] L. Li, K. Sun, C. Kurdak, and J. W. Allen, *Nat. Rev. Phys.* **2**, 463 (2020).
- [14] B. S. Tan, Y.-T. Hsu, B. Zeng, M. C. Hatnean, N. Harrison, Z. Zhu, M. Hartstein, M. Kiourlappou, A. Srivastava, M. D. Johannes, T. P. Murphy, J.-H. Park, L. Balicas, G. G. Lonzarich, G. Balakrishnan, and S. E. Sebastian, *Science* **349**, 287 (2015).
- [15] G. Li, Z. Xiang, F. Yu, T. Asaba, B. Lawson, P. Cai, C. Tinsman, A. Berkley, S. Wolgast, Y. S. Eo, D.-J. Kim, C. Kurdak, J. W. Allen, K. Sun, X. H. Chen, Y. Y. Wang, Z. Fisk, and L. Li, *Science* **346**, 1208 (2014).
- [16] S. M. Thomas, X. Ding, F. Ronning, V. Zapf, J. D. Thompson, Z. Fisk, J. Xia, and P. F. S. Rosa, *Phys. Rev. Lett.* **122**, 166401 (2019).
- [17] N. Wakeham, P. F. S. Rosa, Y. Q. Wang, M. Kang, Z. Fisk, F. Ronning, and J. D. Thompson, *Phys. Rev. B* **94**, 035127 (2016).
- [18] T. Caldwell, A. P. Reyes, W. G. Moulton, P. L. Kuhns, M. J. R. Hoch, P. Schlottmann, and Z. Fisk, *Phys. Rev. B* **75**, 075106 (2007).
- [19] P. Schlottmann, *Phys. Rev. B* **90**, 165127 (2014).
- [20] P. K. Biswas, Z. Salman, T. Neupert, E. Morenzoni, E. Pomjakushina, F. von Rohr, K. Conder, G. Balakrishnan, M. C. Hatnean, M. R. Lees, D. M. Paul, A. Schilling, C. Baines, H. Luetkens, R. Khasanov, and A. Amato, *Phys. Rev. B* **89**, 161107(R) (2014).
- [21] P. K. Biswas, M. Legner, G. Balakrishnan, M. C. Hatnean, M. R. Lees, D. M. Paul, E. Pomjakushina, T. Prokscha, A. Suter, T. Neupert, and Z. Salman, *Phys. Rev. B* **95**, 020410(R) (2017).
- [22] W. A. Phelan, S. M. Koohpayeh, P. Cottingham, J. A. Tutmaher, J. C. Leiner, M. D. Lumsden, C. M. Lavelle, X. P. Wang, C. Hoffmann, M. A. Siegler, N. Haldolaarachchige, D. P. Young, and T. M. McQueen, *Sci. Rep.* **6**, 20860 (2016).
- [23] M. E. Valentine, S. Koohpayeh, W. A. Phelan, T. M. McQueen, P. F. Rosa, Z. Fisk, and N. Drichko, *Phys. B: Condens. Matter* **536**, 60 (2018).
- [24] M. Orendáč, S. Gabáni, G. Pristáš, E. Gažo, P. Diko, P. Farkašovský, A. Levchenko, N. Shitsevalova, and K. Flachbart, *Phys. Rev. B* **96**, 115101 (2017).
- [25] O. Erten, P.-Y. Chang, P. Coleman, and A. M. Tsvelik, *Phys. Rev. Lett.* **119**, 057603 (2017).
- [26] S. Sen, N. S. Vidhyadhiraja, E. Miranda, V. Dobrosavljević, and W. Ku, *Phys. Rev. Research* **2**, 033370 (2020).
- [27] H. Shen and L. Fu, *Phys. Rev. Lett.* **121**, 026403 (2018).
- [28] M. Takigawa, H. Yasuoka, Y. Kitaoka, T. Tanaka, H. Nozaki, and Y. Ishizawa, *J. Phys. Soc. Jpn.* **50**, 2525 (1981).
- [29] P. S. Riseborough, *Ann. Phys.* **9**, 813 (2000).
- [30] P. F. S. Rosa and Z. Fisk, Flux methods for growth of intermetallic single crystals, in *Crystal Growth of Intermetallics*, edited by P. Gille and Y. Grin (De Gruyter, Berlin, Boston, 2018), pp. 49–60.
- [31] J. C. Souza, P. F. S. Rosa, J. Sichelschmidt, M. Carlone, P. A. Venegas, M. O. Malcolms, P. M. Menegasso, R. R. Urbano, Z. Fisk, and P. G. Pagliuso, *Phys. Rev. Research* **2**, 043181 (2020).
- [32] T. Plefka, *Phys. Status Solidi B* **55**, 129 (1973).
- [33] P. Urban, D. Davidov, B. Elschner, T. Plefka, and G. Sperlich, *Phys. Rev. B* **12**, 72 (1975).
- [34] P. A. Venegas, F. A. Garcia, D. J. Garcia, G. G. Cabrera, M. A. Avila, and C. Rettori, *Phys. Rev. B* **94**, 235143 (2016).
- [35] J. G. S. Duque, R. R. Urbano, P. A. Venegas, P. G. Pagliuso, C. Rettori, Z. Fisk, and S. B. Oseroff, *Phys. Rev. B* **76**, 125114 (2007).
- [36] S. E. Barnes, *Adv. Phys.* **30**, 801 (1981).
- [37] A. Abragam and B. Bleaney, *Electron Paramagnetic Resonance of Transition Ions*, Oxford Classic Texts in the Physical Sciences (Oxford University Press, Oxford, 2012).
- [38] C. Kittel, *Quantum Theory of Solids*, 2nd ed. (Wiley, New York, 1985).
- [39] M. Cabrera-Baez, W. Iwamoto, E. T. Magnavita, J. M. Osorio-Guillén, R. A. Ribeiro, M. A. Avila, and C. Rettori, *J. Phys.: Condens. Matter* **26**, 175501 (2014).
- [40] G. Feher and A. F. Kip, *Phys. Rev.* **98**, 337 (1955).
- [41] F. J. Dyson, *Phys. Rev.* **98**, 349 (1955).
- [42] G. G. Lesseux, P. F. S. Rosa, Z. Fisk, P. Schlottmann, P. G. Pagliuso, R. R. Urbano, and C. Rettori, *AIP Adv.* **7**, 055709 (2017).
- [43] J. Stankiewicz, J. Blasco, P. Schlottmann, M. C. Hatnean, and G. Balakrishnan, *arXiv:2109.05313*.
- [44] C. Tsallis and D. A. Stariolo, *Physica A* **233**, 395 (1996).
- [45] N. J. Laurita, C. M. Morris, S. M. Koohpayeh, P. F. S. Rosa, W. A. Phelan, Z. Fisk, T. M. McQueen, and N. P. Armitage, *Phys. Rev. B* **94**, 165154 (2016).
- [46] N. Laurita, C. Morris, S. Koohpayeh, W. Phelan, T. McQueen, and N. Armitage, *Phys. B: Condens. Matter* **536**, 78 (2018).
- [47] J. C. Souza, M. König, M. V. Ale Crivillero, M. O. Malcolms, R. R. Urbano, Z. Fisk, P. F. S. Rosa, P. G. Pagliuso, S. Wirth, and J. Sichelschmidt, *Phys. Rev. Research* **3**, 033016 (2021).
- [48] T. Gambke, B. Elschner, and L. L. Hirst, *Phys. Rev. Lett.* **40**, 1290 (1978).
- [49] Z. F. Priscila F. S. Rosa, Bulk and surface properties of SmB<sub>6</sub>, in *Rare-Earth Borides*, 1st ed., edited by D. Inosov (Jenny Stanford Publishing, Dubai, UAE, 2021), p. 59.
- [50] P. A. Venegas and G. E. Barberis, *Phys. Rev. B* **46**, 911 (1992).
- [51] J. Koringa, *Physica* **16**, 601 (1950).
- [52] G. E. Barberis, D. Davidov, C. Rettori, and J. F. Suassuna, *Phys. Rev. B* **19**, 2385 (1979).
- [53] R. R. Urbano, C. Rettori, G. E. Barberis, M. Torelli, A. Bianchi, Z. Fisk, P. G. Pagliuso, A. Malinowski, M. F. Hundley, J. L. Sarrao, and S. B. Oseroff, *Phys. Rev. B* **65**, 180407(R) (2002).
- [54] R. R. Urbano, P. G. Pagliuso, C. Rettori, P. Schlottmann, J. L. Sarrao, A. Bianchi, S. Nakatsuji, Z. Fisk, E. Velazquez, and S. B. Oseroff, *Phys. Rev. B* **71**, 184422 (2005).
- [55] D. Davidov, K. Maki, R. Orbach, C. Rettori, and E. Chock, *Solid State Commun.* **12**, 621 (1973).
- [56] P. A. Alekseev, A. S. Ivanov, B. Dorner, H. Schober, K. A. Kikoin, A. S. Mishchenko, V. N. Lazukov, E. S. Konvalova, Y. B. Paderno, A. Y. Romyantsev, and I. P. Sadikov, *Europhys. Lett.* **10**, 457 (1989).
- [57] E. Zirngiebl, S. Blumenröder, R. Mock, and G. Güntherodt, *J. Magn. Magn. Mater.* **54–57**, 359 (1986).
- [58] M. Batkova and I. Batko, Effect of valence fluctuations on the ground state properties of SmB<sub>6</sub>, *arXiv:1608.02356*.
- [59] P. Alekseev, J.-M. Mignot, J. Rossat-Mignod, V. Lazukov, and I. Sadikov, *Phys. B: Condens. Matter* **186–188**, 384 (1993).
- [60] W. T. Fuhrman, J. Leiner, P. Nikolić, G. E. Granroth, M. B. Stone, M. D. Lumsden, L. DeBeer-Schmitt, P. A. Alekseev,



- J.-M. Mignot, S. M. Koohpayeh, P. Cottingham, W. A. Phelan, L. Schoop, T. M. McQueen, and C. Broholm, *Phys. Rev. Lett.* **114**, 036401 (2015).
- [61] O. Peña, D. E. MacLaughlin, M. Lysak, and Z. Fisk, *J. Appl. Phys.* **52**, 2152 (1981).
- [62] D. C. Cook, *Z. Naturforsch., A: Phys. Sci.* **51**, 368 (1996).
- [63] S. Tsutsui, R. Masuda, Y. Kobayashi, Y. Yoda, K. Mizuuchi, Y. Shimizu, H. Hidaka, T. Yanagisawa, H. Amitsuka, F. Iga, and M. Seto, *J. Phys. Soc. Jpn.* **85**, 083704 (2016).
- [64] S. Tsutsui, M. Mizumaki, and Y. Kobayashi, *Hyperfine Interact.* **240**, 84 (2019).
- [65] A. Stern, D. K. Efimkin, V. Galitski, Z. Fisk, and J. Xia, *Phys. Rev. Lett.* **116**, 166603 (2016).
- [66] B. Casas, A. Stern, D. K. Efimkin, Z. Fisk, and J. Xia, *Phys. Rev. B* **97**, 035121 (2018).
- [67] R. Calvo, M. C. G. Passeggi, and M. Tovar, *Phys. Rev. B* **4**, 2876 (1971).
- [68] B. G. Wybourne, *Phys. Rev.* **148**, 317 (1966).
- [69] G. Racah, *Phys. Rev.* **63**, 367 (1943).